



In situ observation of ultrasonic cavitation-induced fragmentation of the primary crystals formed in Al alloys



Feng Wang^{a,*}, Iakovos Tzanakis^b, Dmitry Eskin^{c,d}, Jiawei Mi^e, Thomas Connolley^f

^a Brunel Centre for Advanced Solidification Technology (BCAST), Brunel University London, Uxbridge UB8 3PH, UK

^b Faculty of Technology, Design and Environment, Oxford Brookes University, Wheatley Campus, Wheatley OX33 1HX, UK

^c Brunel Centre for Advanced Solidification Technology (BCAST), Brunel University London, Uxbridge UB8 3PH, UK

^d Tomsk State University, Tomsk 634050, Russia

^e School of Engineering & Computer Science, University of Hull, Hull, East Yorkshire HU6 7RX, UK

^f Diamond Light Source Ltd, Harwell Science & Innovation Campus, Didcot OX11 0DE, UK

ARTICLE INFO

Keywords:

Aluminium alloy

Ultrasonic processing

Primary crystals

Fragmentation mechanism

Cavitation

In situ high speed imaging

ABSTRACT

The cavitation-induced fragmentation of primary crystals formed in Al alloys were investigated for the first time by high-speed imaging using a novel experimental approach. Three representative primary crystal types, Al₃Ti, Si and Al₃V with different morphologies and mechanical properties were first extracted by deep etching of the corresponding Al alloys and then subjected to ultrasonic cavitation processing in distilled water. The dynamic interaction between the cavitation bubbles and primary crystals was imaged *in situ* and in real time. Based on the recorded image sequences, the fragmentation mechanisms of primary crystals were studied. It was found that there are three major mechanisms by which the primary crystals were fragmented by cavitation bubbles. The first one was a slow process via fatigue-type failure. A cyclic pressure exerted by stationary pulsating bubbles caused the propagation of a crack pre-existing in the primary crystal to a critical length which led to fragmentation. The second mechanism was a sudden process due to the collapse of bubbles in a passing cavitation cloud. The pressure produced upon the collapse of the cloud promoted rapid monotonic crack growth and fast fracture in the primary crystals. The third observed mechanism was normal bending fracture as a result of the high pressure arising from the collapse of a bubble cloud and the crack formation at the branch connection points of dendritic primary crystals. The fragmentation of dendrite branches due to the interaction between two freely moving dendritic primary crystals was also observed. A simplified fracture analysis of the observed phenomena was performed. The specific fragmentation mechanism for the primary crystals depended on their morphology and mechanical properties.

1. Introduction

Ultrasonic melt processing (USP) is the application of ultrasonic waves with intensity above a certain threshold to liquid or semi-solid metal alloys; it has attracted considerable interest from the solidification research communities and casting industry. USP has been demonstrated to have significant benefits in microstructural refinement for dendritic grains and primary intermetallic particles, while also reducing porosity and improving the quality of castings [1–3].

Primary crystals are formed in aluminium alloys at certain concentrations of alloying elements and sometimes are desirable (e.g. primary Si for wear and thermal stability control or Al₃Ti and Al₃Zr for grain size control [1]) and sometimes are not (e.g. large primary Al₃Zr or Al₃V crystals in wrought alloys). In any case, it is desirable to have

these primary crystals in a compact shape and fine sizes. USP is one of the means of achieving this [4]. The specific mechanisms of how USP works are largely unknown and general considerations of nucleation and fragmentation are used. The latter is the focus of this paper.

Since the 1950s, many dedicated USP solidification experiments had been carried out and used various *ex-situ* (i.e. after the solidification experiments) characterisation methods to analyse the materials produced by USP. In the past few years, research in this field has moved onto using *in situ* (i.e. during the solidification experiments) characterisation techniques to the effects of USP on the solidification microstructures in real time [5–13]. In terms of the experimental techniques and materials used, they can be grouped into two categories: (i) optical imaging of transparent analogue alloys, and (ii) synchrotron X-ray imaging of real metallic alloys. Early *in situ* studies [5,6] of the

* Corresponding author.

E-mail addresses: feng.wang@brunel.ac.uk (F. Wang), itzanakis@brookes.ac.uk (I. Tzanakis), dmitry.eskin@brunel.ac.uk (D. Eskin), j.mi@hull.ac.uk (J. Mi), thomas.connolley@diamond.ac.uk (T. Connolley).

<http://dx.doi.org/10.1016/j.ultsonch.2017.03.057>

Received 17 January 2017; Received in revised form 6 March 2017; Accepted 20 March 2017

Available online 09 April 2017

1350-4177/ © 2017 The Author(s). Published by Elsevier B.V. This is an open access article under the CC BY license (<http://creativecommons.org/licenses/by/4.0/>).

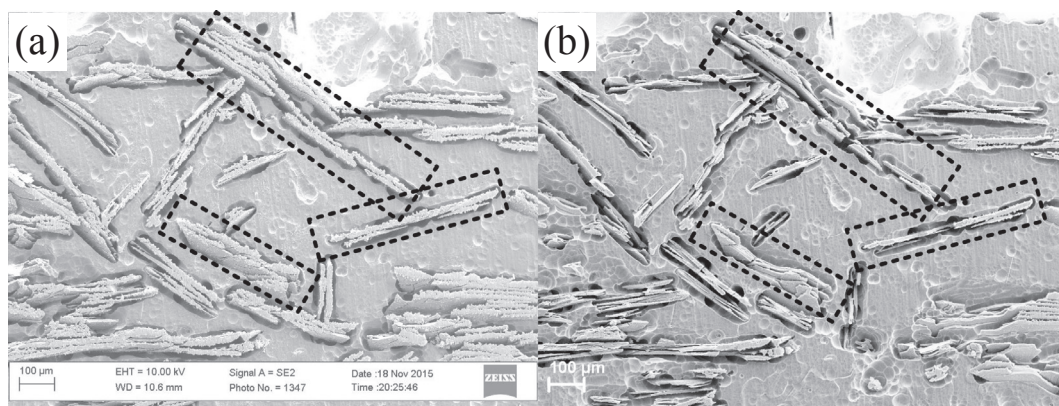


Fig. 1. Typical SEM micrographs of the primary Al_3Ti crystals (a) deeply etched sample without USP; (b) deeply etched sample after 10 s USP in water with the input power of 100 W.

solidification of transparent analogue alloys under the influence of ultrasound showed that grain nucleation was indeed enhanced by ultrasonic vibration and the fragmentation of a growing dendrite was promoted by the oscillation of quasi-steady bubbles and the collapse of transient bubbles. Images and videos from Ref. [7] on the breakage of calcite crystals suspended in a saturated CaCO_3 solution demonstrated that the collapse of cavitation bubble clusters caused the fracture and destruction of suspended calcite crystals. Shu et al. [8] demonstrated that the fragmentation of dendrites in a transparent analogue alloy could progress slowly or violently depending on the type of cavitation bubbles. Most recently, synchrotron X-ray imaging has been extensively applied to *in situ* studies of various aspects of solidification of real metals and alloys, also under the effect of various external fields [14–18]. Using synchrotron X-ray radiography, Huang et al. [11], Mi et al. [19] and Xu et al. [13] measured the size distribution, average radius and growth rate of cavitation bubbles in an Al-10 wt% Cu alloy. In addition, Tzanakis et al. [12] observed the instantaneous re-filling of a micro-capillary channel with melt in an Al-10 wt% Cu alloy, which provides direct evidence for the ultrasonic capillary effect. Tan et al. [10] observed shockwaves and enhanced flows in a Bi-8 wt% Zn alloy. However, there are still only a few reports on the *in situ* observation of direct interaction between cavitation bubbles with the real solid phases (either dendrites or primary intermetallic particles) from metallic alloys, mainly because of the experimental difficulty in capturing the very transient phenomena of the interactions between the cavitation bubbles and the growing solid phases in the liquid metal in the same view field (often limited to a view field of less than 2 mm^2 in a synchrotron X-ray imaging experiment). In order to fully understand the highly dynamic behaviour of the cavitation bubbles and their interactions with the growing solid phases, real-time images with sufficient temporal (imaging speed) or spatial (image resolution) resolution are still needed.

Furthermore, it is obvious that the mechanical properties, especially the strength and toughness, of different solid phases (e.g. dendrites of metallic alloys or analogue alloys, molecular crystals or intermetallic particles) also play a significant role in determining whether the phases would be fractured or not during USP.

In this paper, a simple and effective experimental methodology was developed to directly observe the real time interactions between cavitation bubbles and the primary crystals formed in Al alloys. Primary crystals with different mechanical properties and morphologies were selected, extracted from corresponding binary Al alloys and then subjected to USP in water and imaged *in situ* using high-speed filming. Based on the images extracted from the recordings, the mechanisms of cavitation-induced fragmentation are discussed and elucidated by taking into account of the mechanical properties and morphologies of the primary crystals.

We believe that the results obtained are relevant to the mechanisms of fragmentation in liquid aluminium as well. The cavitation evolves in

water and liquid aluminium in a similar way [20,21] with the pressures produced by collapsing cavitation bubbles being higher in liquid Al. Therefore, the cavitation fragmentation resulting from cavitation in water should be similar or even more pronounced in liquid Al. There is always an issue of the mechanical properties of the crystals subjected to the cavitation action. As we will show later in this paper, the mechanical properties of intermetallics are rarely available even for room temperature and are almost unknown at the temperatures of liquid Al alloys, which makes the analysis of the observations very difficult indeed. We have decided to use whatever data are available to analyse our observations, i.e. room temperature properties for room temperature observations. The analysis has generic value of its own. Our results also demonstrate for the first time that the fragmentation of primary crystals in Al alloys is actually possible by cavitation. The extension of our observations to melt conditions requires further work using *in situ* X-ray imaging, coupled with a highly-sophisticated experimental technique to measure the high-temperature properties of intermetallics. Such experimental work is currently underway in the participating institutions.

2. Experimental methodology

2.1. Materials and sample preparation

Primary Si, Al_3Ti , and Al_3V were selected as three representative primary crystals of different morphologies (faceted block, plate and dendrite, respectively) formed in Al alloys. In order to extract these primary crystals, samples of the dimension of $20 \text{ mm} \times 20 \text{ mm} \times 15 \text{ mm}$ were first cut from an Al-0.4 wt% Ti alloy solidified in a graphite crucible, commercial Al-20 wt% Si and Al-10 wt% V master alloys (KBM Master Alloys B.V.) respectively. The detailed casting conditions and sampling positions for the Al-0.4 wt% Ti alloy can be found in Ref. [22]. Then, the samples were deeply etched by a 10 wt% NaOH water solution for about 2 h. The deeply-etched samples were examined in a scanning electron microscope (SEM, ZEISS SUPRA 35VP) to observe the primary crystals. Fig. 1(a) shows a typical SEM image of an Al-0.4 wt% Ti alloy sample after deep etching. The primary Al_3Ti crystals clearly stick out from the Al matrix surface with part of the crystals still embedded in the Al matrix. Similarly, primary Si (from Al-20 wt% Si) and Al_3V (from Al-10 wt% V) crystals were also observed to protrude from the Al matrix surface after deep etching.

2.2. Experimental setup and procedures

Each deep-etched sample was gently rinsed in water and then fixed by adhesive to the bottom of a small transparent plastic tank ($70 \text{ mm} \times 30 \text{ mm} \times 40 \text{ mm}$) close to the front wall. The plastic tank was then filled with distilled water and placed on a movable stage for USP using an UP200S ultrasonic processor (Hielscher, 24 kHz, adjus-

table input power from 40 W to 200 W) which was connected to a titanium sonotrode with a tip diameter of 1 mm. Note that the power values indicate the electric power and the detailed technical data of the ultrasonic processor and sonotrode can be found in the instruction manual [23]. The sonotrode tip was positioned approximately 4 mm above the top surface of the sample. During experiments, the water temperature was kept constant at 25 °C. After USP, the sample was again examined by SEM. Fig. 1(b) presents a SEM micrograph of the same position of the same sample as in Fig. 1(a) but after USP. A simple comparison of Fig. 1(a) and (b) clearly shows that the primary Al₃Ti crystals highlighted by dashed lines were fragmented by ultrasonic cavitation.

The detailed interactions between the cavitation bubbles and the protruding primary crystals were recorded *in situ* with a high-speed camera (Vision Research Phantom V7.3) that is capable of operating at 222, 222 frames per second (fps). The greater is the filming speed, the more light is required for getting distinct images, and the smaller is the frame size. Therefore, the actual imaging was done at the optimum fps rate possible for a particular set up. The camera was also equipped with either a 4× (Schneider) or a 10× (Sill) optical lens. High speed imaging of the interactions between cavitation bubbles and primary crystals was facilitated by pre-focusing the camera on selected primary crystals protruding from the Al matrix. The drawback of high magnification optical imaging is a shallow depth of focus, so pre-focusing on particles fixed in the matrix increased the likelihood of capturing good quality images, compared to trying to image fragmentation of free-circulating particles suspending in water. A high-power, constant intensity, light source (Karl Storz Power LED 175) provided front illumination for filming. Front illumination was used because the primary crystals protruding with inclined angles reflected light towards the camera, making it possible to have bright images of the primary crystals by appropriately adjusting the projection angle of the light source. Fig. 2 is a schematic diagram showing the experimental setup.

For each type of crystal, at least 20 particles with fragmentation have been observed and their behaviour under cavitation recorded. These observations showed consistency and repeatability of the phenomena demonstrated and discussed below. For brevity, only the representative and most illustrative series of images (and videos in Supplemental material) are given in the paper.

3. Results and discussion

3.1. Fragmentation of primary Al₃Ti crystals

Fig. 3 shows a series of images extracted from a sequence recorded as a primary Al₃Ti crystal was fragmented by a stationary, pulsating

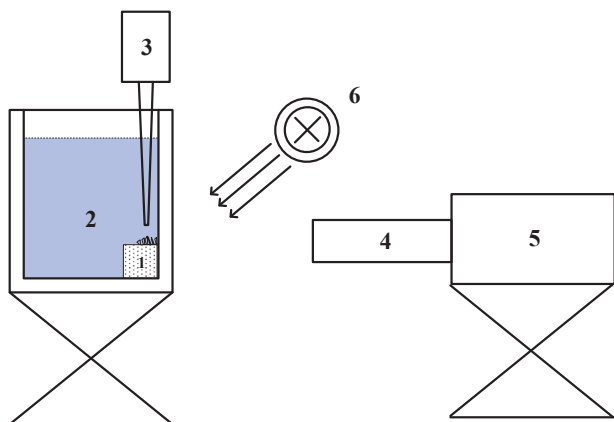


Fig. 2. A schematic of the experimental setup consisting of: (1) deeply etched sample, (2) transparent tank, (3) ultrasonic processor and sonotrode, (4) macro lens, (5) high-speed camera, and (6) high-power light source.

cavitation bubble. For brevity, only a few images are shown to elucidate the fragmentation process. A supplementary video corresponding to the sequence of images (File name: [Supplementary video 001](#)) is available with online version of the paper. The first frame ($t = 0 \mu\text{s}$) shows a typical primary Al₃Ti crystal of dendritic-plate morphology (dimensions: about $220 \mu\text{m} \times 220 \mu\text{m} \times 10 \sim 20 \mu\text{m}$ as was measured in Ref. [22]) with its broad plane being brightly illuminated. The detailed morphology and dimensions of these primary Al₃Ti crystals can be found in Ref. [22]. In the next frame, a bubble starting expansion was observed, and this bubble continued to expand in the following frames as illustrated in Fig. 3(c) and (d). In fact this bubble was observed pulsating at this position for about 7000 frames = $70,000 \mu\text{s} = 1680$ acoustic cycles. At some moment between frames in Fig. 3(d) and (e), the bubble started to lose stability and only a blurred bubble was observed, with its outline highlighted by a dashed line in Fig. 3(e). The pronounced difference in the visual sharpness of the bubble during the stable and instable phases indicates that the contraction was too fast to be captured by the camera settings (imaging speed = 100,000 fps with the exposure time = $8 \mu\text{s}$), implying that the bubble was possibly experiencing an implosive collapse. In Fig. 3(f), a clear crack throughout the primary Al₃Ti crystal from left to right appeared as the bubble continued to contract. From this moment and until the final fragmentation one can observe cyclic bending movement of the upper part of the crystal, indicative of cyclic loading. Following that, the crack became more distinct and the primary Al₃Ti crystal was completely fragmented as indicated by the arrows in Fig. 3(g). It seems that the final fragmentation of the primary Al₃Ti crystal was closely related to the collapse of the pulsating bubble. Further pulsation of the re-bound bubble slowly pushed the broken primary Al₃Ti crystal fragment away as shown in Fig. 3(h). Note that the primary Al₃Ti crystal underwent 1680 cycles of bubble pulsation before it was eventually fragmented by the last cycle of bubble expansion and collapse. This indicates that the crack formation and propagation in this primary Al₃Ti crystal is likely to be related to the fatigue mechanism due to the cyclic acoustic pressure exerted by the pulsating bubble during its expansion, contraction, implosion and rebounding phases. The final fracture was brittle and resulted from the implosion of a cavitation bubble. The height (h) of the pulsating bubble for 10 acoustic cycles was roughly measured based on the extracted images as illustrated in Fig. 3(b), (c) and (d) and the values are presented together with the cyclic acoustic pressure at the sonotrode tip as shown in Fig. 4. The acoustic pressure at the sonotrode tip was calculated using the following formula (1)

$$P_a = P_A \cos(\omega t), \quad (1)$$

where $P_A = \sqrt{2\rho CW/A}$ is the amplitude of the imposed ultrasound wave determined by the input ultrasound power W (60 W), the area of the emitting surface A (the 1-mm diameter tip has an emitting area of $7.85 \times 10^{-7} \text{ m}^2$), the density ρ (1 kg/m^3) and sound speed C in water (1482 m/s) and angular frequency $\omega = 2\pi f$ where f (24 kHz) is the frequency of ultrasound wave. It appears from Fig. 4 that the measured running height of the pulsating cavitation bubble is largely in antiphase with the calculated acoustic pressure, as one would expect. With a typical cavitation threshold in water of 0.1–0.2 MPa [1], the acoustic conditions in our experiments reflect developed cavitation.

In addition to the fragmentation by a stationary pulsating bubble via the mechanism of fatigue fracture, another mechanism of fragmentation of primary Al₃Ti crystal by a flowing bubble cloud was also recorded at USP power of 200 W. What we call “bubble cloud” is a blurry image that may represent a cluster/avalanche of small bubbles. Indication for this scenario is a fuzzy mist around the intermetallic surface in some recording like in Fig. 5 (online video resembles to an avalanche passing through the field of view). These clusters can travel and transport bubbles across the longitudinal direction of the ultrasonic waves where they may implode, rebound and multiply as well as emit micro-jets and powerful shockwaves during the process. To resolve specific features of the bubble cloud is beyond the limits of state-of-the-

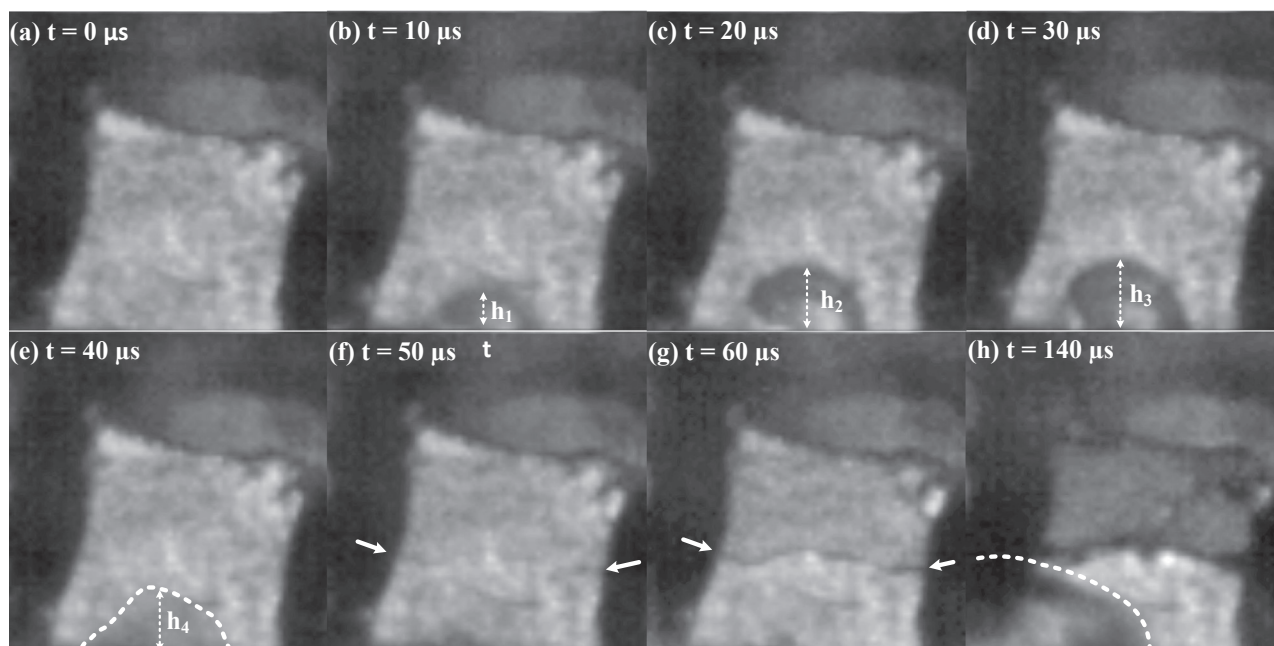


Fig. 3. Images of a pulsating cavitation bubble, causing fragmentation of a primary Al_3Ti crystal. The field of view is $337.28 \times 337.28 \mu\text{m}^2$ and the images were recorded at 1×10^5 fps. This video is available with the online version of the paper as [supplementary video 001](#).

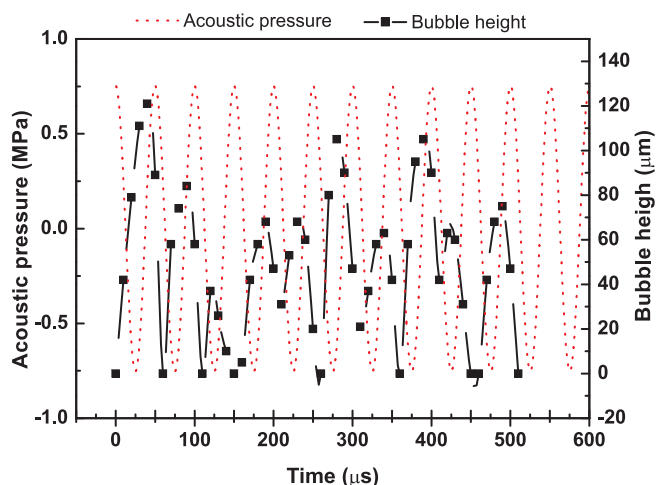


Fig. 4. The variation of the measured height of the cavitation bubble along with the calculated acoustic pressure at the sonotrode tip.

art imaging technique that we have used. However, more in-depth information on cluster formation can be found in Ref. [24]. One of the typical series of images is shown in Fig. 5. A supplementary video corresponding to this sequence of images (File name: [Supplementary video 002](#)) is available with online version of the paper. In Fig. 5(a), an evident primary Al_3Ti crystal with one arm corner protruding out of the Al matrix is observed. A bubble cloud flowing downwards to the arm corner is also highlighted by an arrow. The reason why the bubble cloud is blurry may be that: (i) the bubble cloud was three dimensional and also possibly travelling in the direction perpendicular to the image plane while the lens could only focus on the image plane with the rest of the bubble cloud out of the focus; (ii) the dynamic behaviour of the small bubbles comprising the bubble cloud was too fast to be captured by the current camera settings of 36,036 fps (exposure time = $25.75 \mu\text{s}$). Basically, the image is the average of the dynamic behaviour of the bubble cloud over the exposure time. Although the camera used in the present work can be operated at 222,222 fps, there has to be always a compromise among imaging speed, exposure time, image resolution, and the field of view. Fig. 5(b) clearly shows that the

bubble cloud was approaching the arm corner with the front approximately indicated by the arrow. Then, between one frame and the next, part of the arm corner disappeared (Fig. 5(c)) seemingly as a result of direct interaction between the bubble cloud and the protruding arm corner. The trajectory of the broken fragment was not observed, possibly due to the fast movement of the fragment in a direction perpendicular to the image plane which took the fragment out of focus. Finally, the bubble cloud quickly moved out of the field of view as indicated by the trail in Fig. 5(d). Based on four observed frames, the average speed of the bubble cloud was estimated to be ~ 5 m/s, which is fast compared to the typically reported velocities of acoustic streaming that are in the range of cm/s [1,18]. It is important to point out that the primary Al_3Ti crystal survived approximately five similar bubble clouds passing by before it was eventually fragmented by the one as shown in Fig. 5. It appears that, although the fragmentation of primary Al_3Ti crystal was a relatively quick process, it still belonged to the fatigue failure considering that the primary Al_3Ti crystal survived the passage of few bubble clouds before it was fragmented. It is suggested that the preceding bubble clouds facilitated the growth of a sub-critical crack in the crystal to a critical-size crack, after which the crack propagation became dramatically faster as demonstrated in Fig. 5.

3.2. Fragmentation of primary Si crystals

Fig. 6 shows a series of images illustrating a flowing bubble cloud breaking off a primary Si crystal at USP power of 200 W. A supplementary video corresponding to the image sequence (File name: [Supplementary video 003](#)) is available with online version of the paper. Fig. 6(a) presents a well-faceted block of a primary Si crystal with one facet being brightly illuminated. This faceted-block morphology of primary Si after etching away the Al matrix is a common morphology of primary Si found in hypereutectic Al-Si alloys. A bubble cloud flowing down and coming towards the primary Si crystal can be seen at the top left corner of Fig. 6(b) where the blurry patch indicates the moving bubble cloud. In Fig. 6(c) and (d) the bubble cloud approached the primary Si crystal. As the bubble cloud was passing the primary Si crystal, the collapse of the bubbles violently stripped the top piece off the crystal as seen in Fig. 6(e) and (f) and left an obvious crack in the

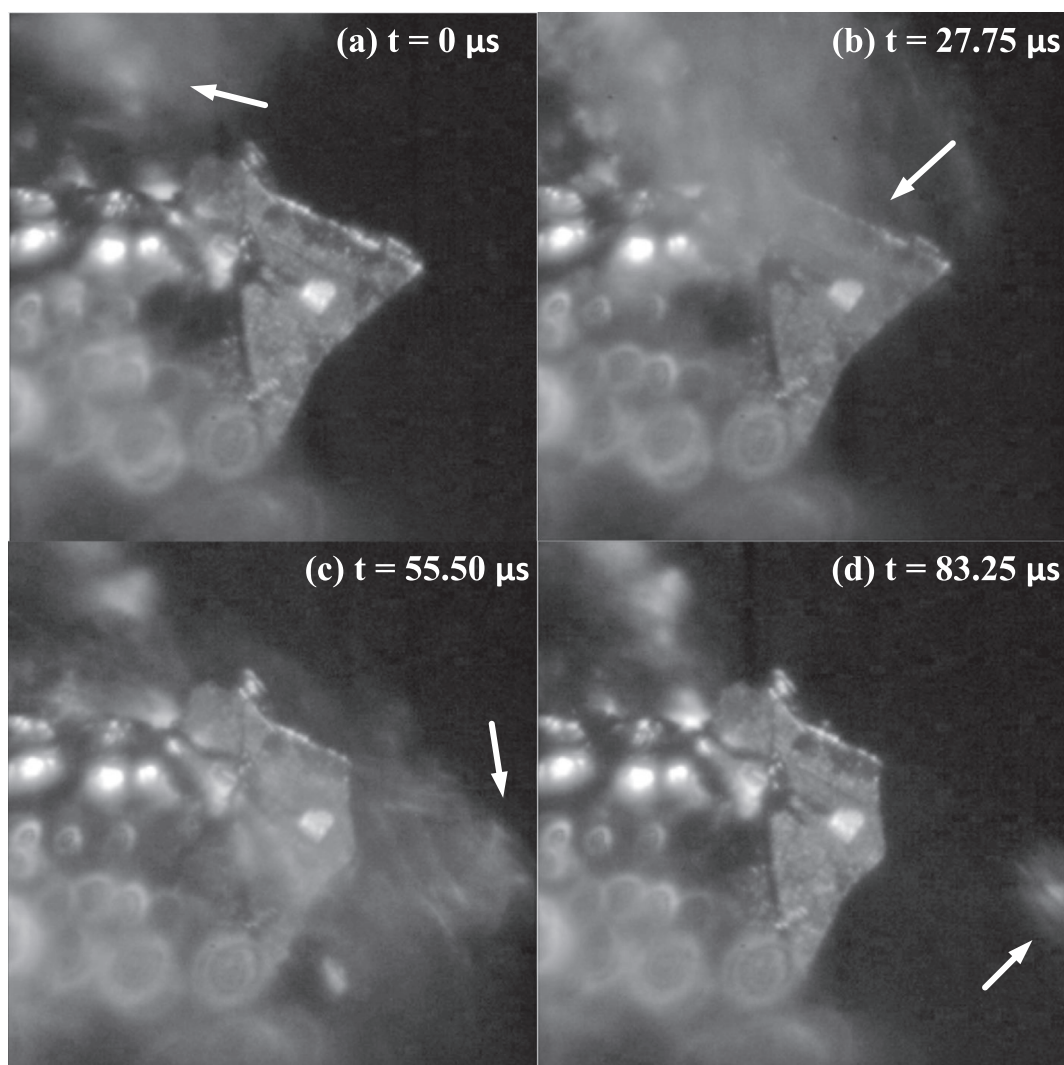


Fig. 5. Images of a primary Al_3Ti crystal fragmented by a flowing bubble cloud. The field of view is $552.96 \times 552.96 \mu\text{m}^2$ and the images were recorded at 36,036 fps. This video is available with the online version of the paper as [supplementary video 002](#).

remaining primary Si crystal as indicated by the arrow in Fig. 6(g) and (h). The subsequent bubble clouds continued to widen the gap between the two parts of the remaining primary Si crystal with clear cyclic movement of these parts, and eventually broke half of the primary Si crystal away, leaving the other half with a typical cleavage surface as shown in Fig. 7. This is probably because the bottom part of the primary Si crystal was still embedded in the Al matrix, making it difficult to fully detach. This fragmentation of the primary Si crystal was quite similar to that of primary Al_3Ti in Fig. 5. Therefore, it is suggested that the fragmentation of primary Si crystal also belongs to the fatigue failure, with gradual crack growth until it reaches the critical size for final fracture. While it may seem surprising that fatigue cracking is possible in a brittle material like silicon, the phenomenon has actually been observed and studied elsewhere, for example by Ikehara and Tsuchiya [25].

3.3. Fragmentation of primary Al_3V crystals

Fig. 8 shows the images of a primary Al_3V crystal before and after USP in water for about 1.28 s with the input power of 200 W. A supplementary video corresponding to the fragmentation process (File name: [Supplementary video 004](#)) is available with online version of the paper. Note that the video is edited from sections by deleting the parts where no apparent fragmentation was observed considering the raw

video file is too long and large to upload. Fig. 8(a) clearly shows a well-grown primary Al_3V dendrite with obvious secondary and even tertiary branching arms. After USP, most of the secondary and tertiary branches were fragmented and stripped off, leaving only the primary Al_3V dendrite trunk as seen in Fig. 8(b). The comparison between Fig. 8(a) and (b) confirms the striking fragmentation effect of USP on intermetallic dendrites. The exact moments of the dendrite fragmentation were also recorded as shown in Figs. 9 and 10.

One of the fragmentation moments when two branches were simultaneously broken by a blast of a bubble cloud is displayed in Fig. 9. The video corresponding to this fragmentation is the first section of the supplementary video (File name: [Supplementary video 004](#)) available with online version of the paper. As we can see in Fig. 9(a), two typical secondary branches growing on the primary trunk are marked by the arrows. In Fig. 9(b), an outlined bubble cloud approached the branches. A branch marked by a dashed arrow was bent by the pressure exerted by the coming bubble cloud. As the bubble cloud interacted with the branches, the branches were fragmented as seen in Fig. 9(c) and particularly in Fig. 9(d) in which the fragments of the branches were broken away as indicated by the arrows. After the bubble cloud left the primary Al_3V crystal dendrite, the two relatively dark blurry fragments were observed as circled in Fig. 9(e), travelling in the direction perpendicular to the image plane and hence moving out of focus. In the following frames, one of the fragments disappeared from

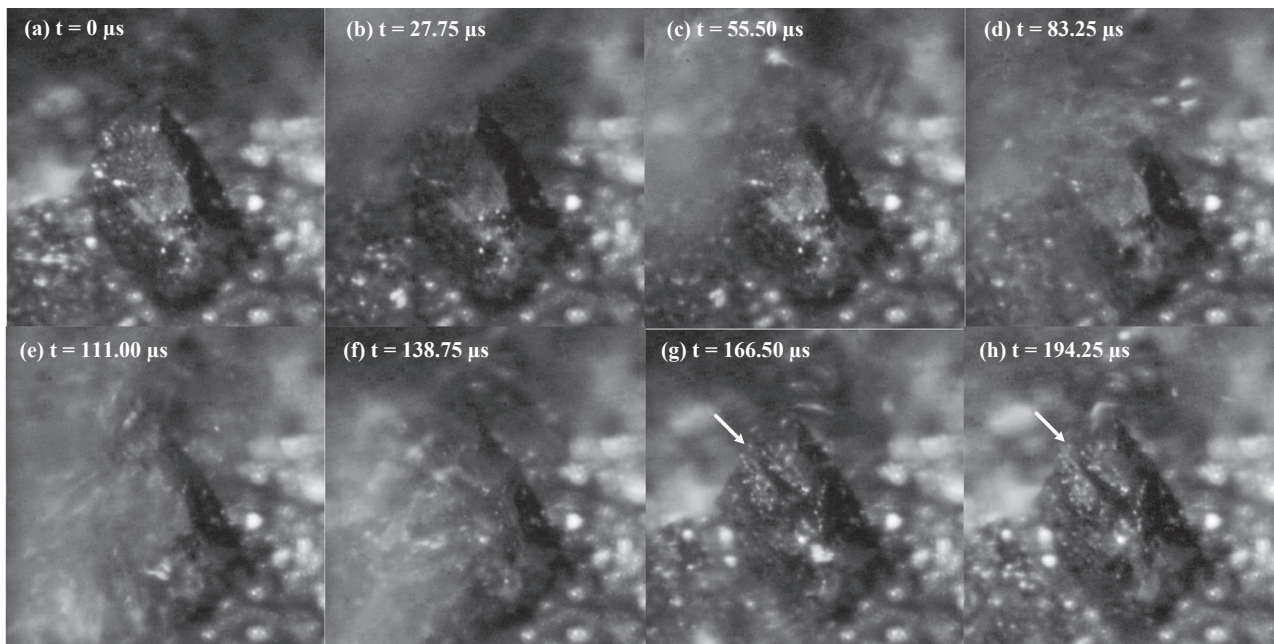


Fig. 6. Images of a primary Si crystal fragmented by a bubble cloud which also stripped a piece off the primary Si crystal. The field of view is $552.96 \times 552.96 \mu\text{m}^2$ and the images were recorded at 36,036 fps. This video is available with the online version of the paper as [supplementary video 003](#).

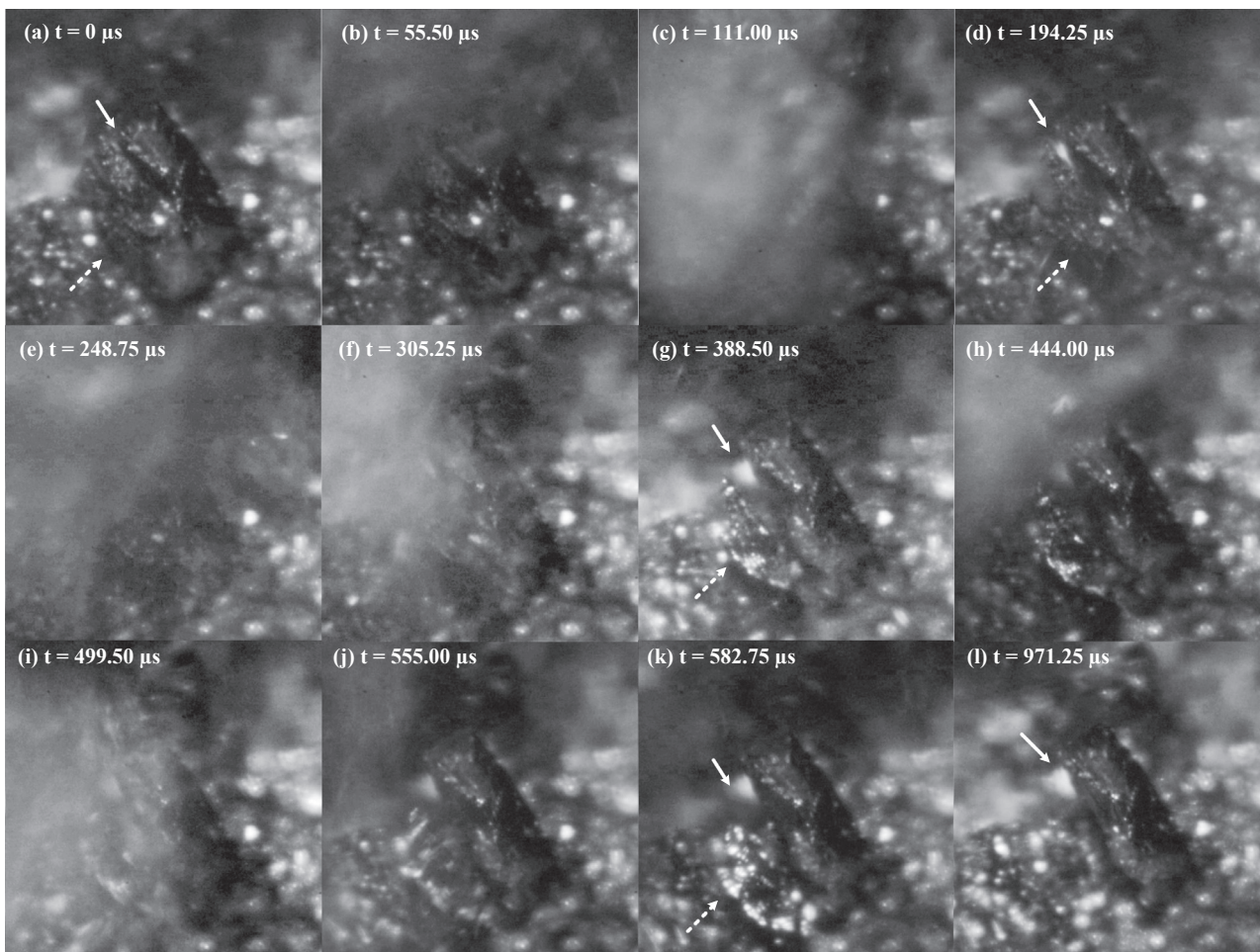


Fig. 7. Images of continuous bubble clouds widening the gap and eventually stripping the fragment away. The field of view is $552.96 \times 552.96 \mu\text{m}^2$ and the images were recorded at 36,036 fps. This video is available with the online version of the paper as [supplementary video 003](#).

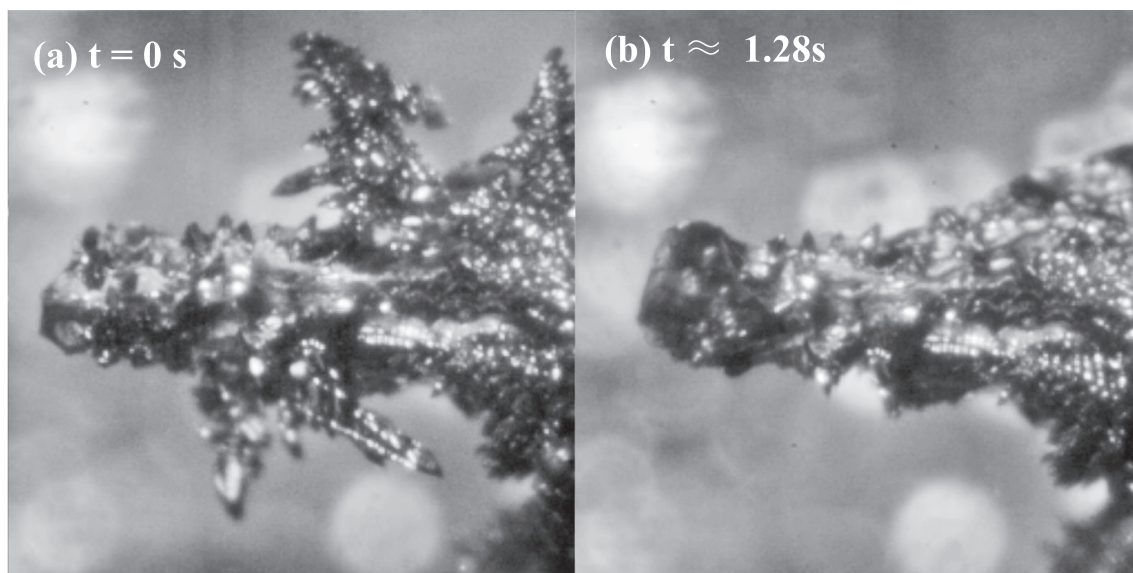


Fig. 8. (a) A well-grown primary Al_3V dendrite before ultrasonic processing in water; (b) the same primary Al_3V dendrite after ultrasonic processing with input power = 200 W in distilled water for around 1.28 s. The field of view is $552.96 \times 552.96 \mu\text{m}^2$. This video is available with the online version of the paper as [supplementary video 004](#).

the field of view and the other one remained visible, as circled in [Fig. 9\(f\)](#), (g) and (h). It is necessary to mention that this fragmentation process occurred upon the start of the ultrasonic processing. In contrast to the above fragmentation scenarios shown in [Figs. 3, 5 and 6](#), the two branches of Al_3V were fragmented when the first bubble cloud interacted with them. It appears that the fragmentation of these two branches by the bubble cloud is more of bending failure, probably due to a notch effect or local thinning at roots resulting from dendrite growth or the deep etching.

Following the fragmentation of the two branches, the fragmentation of another small (possibly tertiary) branch is illustrated in [Fig. 10](#). The video corresponding to this fragmentation is the section marked as *from 195.36 to 196.19 ms* of the supplementary video (File name: [Supplementary video 004](#)) available with online version of the paper. The small branch is marked by an arrow in [Fig. 10\(a\)](#). A bubble cloud approached the small branch as outlined in [Fig. 10\(b\)](#) and (c). As the

bubble cloud was passing by the primary trunk, the small branch rapidly detached off the secondary branch and disappeared from the field of view as seen in [Fig. 10\(d\)](#). As the bubble moved downwards further and left the field of view, a clear view of the remains shows obvious fragmentation of the small branch as pointed by the arrows in [Fig. 10\(e\)](#) and (f). Similar to the fragmentation shown in [Figs. 5 and 6](#), the small branch also experienced oscillations during the passage of more bubble clouds before the actual fragmentation occurred as seen in [Fig. 10](#). As a result, it is also suggested the fragmentation of this small branch belongs to the proposed fatigue failure mechanism.

In addition to the above fragmentation due to the interaction between the acoustic cavitation bubbles and the primary crystals, another fragmentation event occurring between two freely flowing primary Al_3V dendrites (or dendrite fragments) was also recorded, and is illustrated in [Fig. 11](#). A supplementary video corresponding to this (File name: [Supplementary video 005](#)) is available with online version

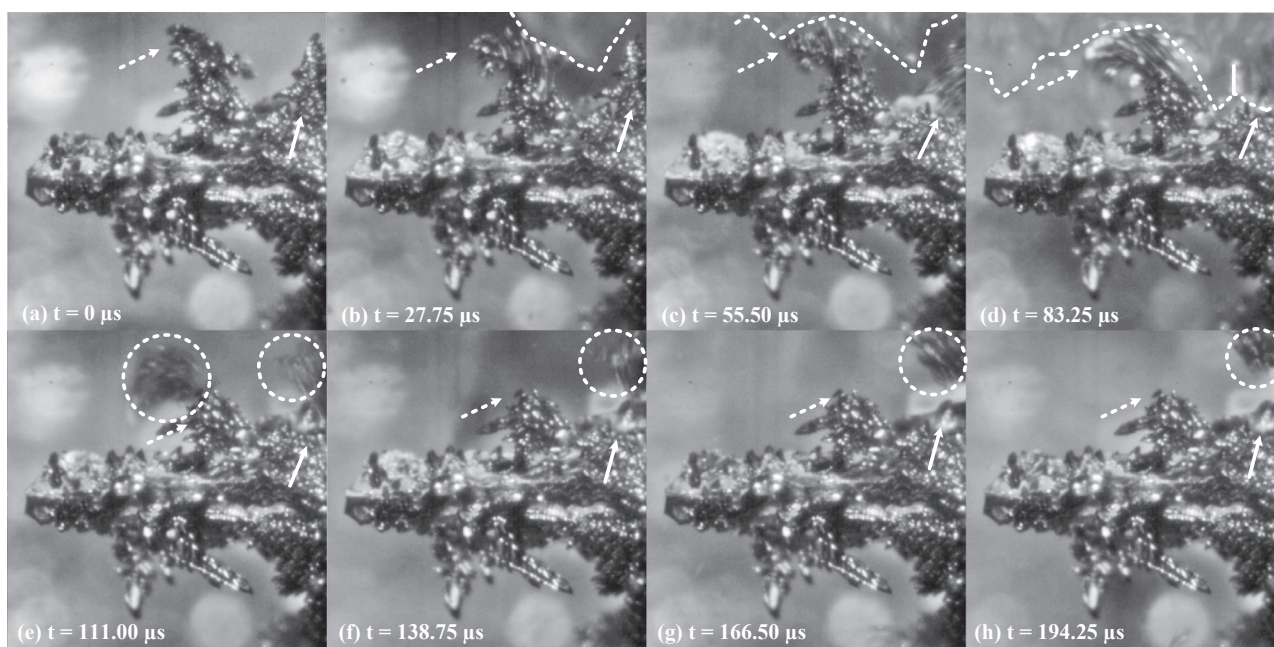


Fig. 9. Images of a flowing bubble cloud breaking two branches simultaneously of a primary Al_3V dendrite. The field of view is $552.96 \times 552.96 \mu\text{m}^2$ and the images were recorded at 36,036 fps. The video corresponding to this fragmentation is the first section of the supplementary video (File name: [Supplementary video 004](#)) available with online version of the paper.

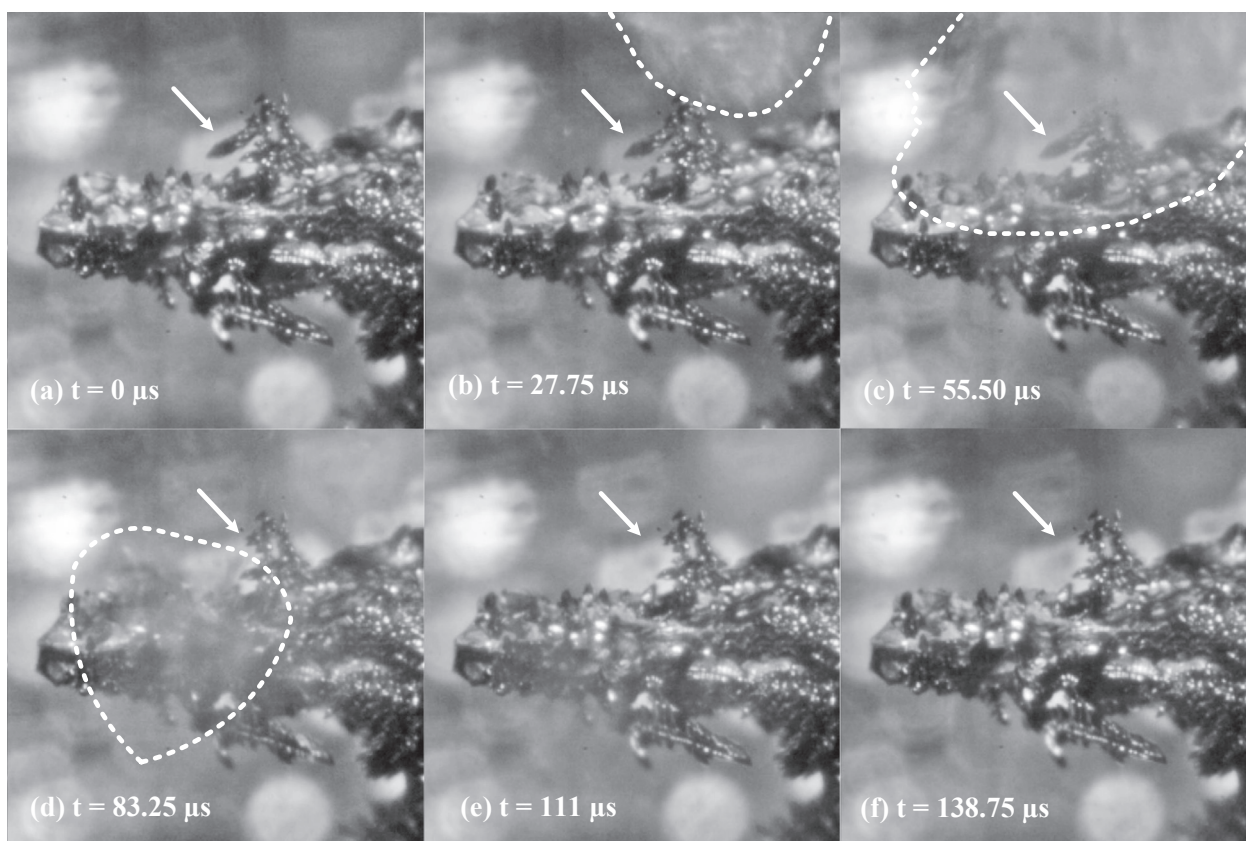


Fig. 10. Images of another flowing bubble cloud detaching a small branch off the remains of the branches after previous fragmentation. The field of view is $552.96 \times 552.96 \mu\text{m}^2$ and the images were recorded at 36,036 fps. The video corresponding to this fragmentation is the section marked as from 195.36 to 196.19 ms of the supplementary video (File name: [Supplementary video 004](#)) available with online version of the paper.

of the paper. As we can see in [Fig. 11\(a\)](#), two Al_3V dendrites (No. I and No. II) are indicated by the dashed and solid arrows, respectively. The spotlight is on No. I primary Al_3V dendrite which consists of three sections as marked by A, B and C. [Fig. 11\(b\)](#), (c) and (d) show the

different views of the two Al_3V dendrites as they were moving and rotating around a pulsating bubble. In particular, Section A of No. I Al_3V dendrite is marked. As the Al_3V dendrites continued to move and interact with each other, Section A of No. I Al_3V dendrite was observed

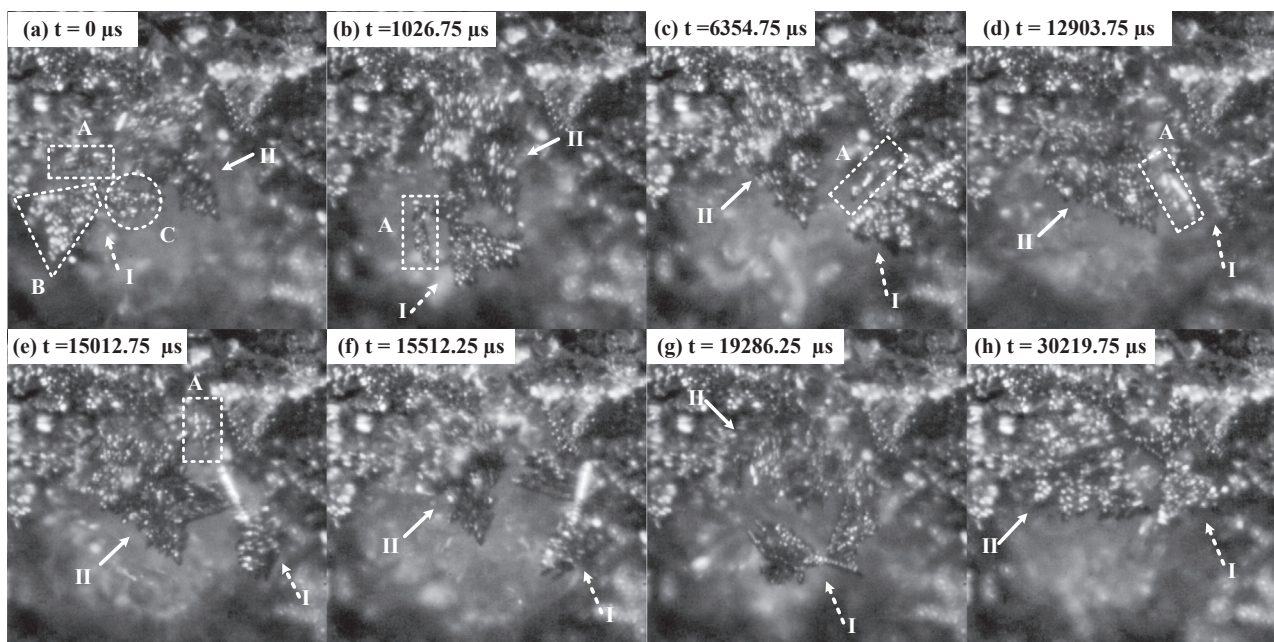


Fig. 11. Images of two primary Al_3V dendrites moving around a pulsating bubble and interacting with each other, eventually leading to fragmentation of a small branch as highlighted by dashed rectangle A. The field of view is $552.96 \times 552.96 \mu\text{m}^2$ and the images were recorded at 36,036 fps. This video is available with the online version of the paper as [supplementary video 005](#).

to fragment and detach from No. I Al_3V dendrite as shown in Fig. 11(e). Further images, i.e., Fig. 11(f), (g) and (h), of No. I Al_3V dendrite show its different views as it rotated with a clear indication that Section A is missing. It is suggested that the continuous interaction (collisions) between the two floating dendrites broke off part of one of the observed Al_3V dendrites. Note that the speed of the two floating Al_3V dendrites was relatively slow and their interaction did not seem to be violent. Despite this, the interaction still caused fragmentation at the weak points of branch connections.

It is interesting to point out here that the authors did not observe any fragmentation due to the expected microjet impingement on the primary crystals. One of the possible reasons may be that the sizes of the primary crystals in the present work are similar to those of the cavitation bubbles, which probably could not incur the formation of a microjet [26]. A higher possibility is that the current camera frame rate and illumination settings were still not good enough to capture the formation of a microjet and its impingement on primary crystals. It is necessary to point out here that the details of the bubble cloud are still not resolved based on the current experimental results/images. There is possibility that these bubble clouds emit micro-jets during the bubble collapse, which is not possible to resolve using the current experimental setup.

3.4. Fracture mechanics

In order to further understand the fragmentation mechanisms, the mechanism of the crack growth preceding the fragmentation is of great importance. Our observations suggest a fatigue mechanism because of (a) observed oscillations of the parts of the crystal with visible crack growth before its fragmentation and (b) cyclic nature of loading by oscillating bubbles. However, due to the lack of sufficient materials data as described in the following, this still requires further work to be done.

In the present paper, nevertheless, a simplified study of the fracture mechanics was performed in an attempt to understand the fragmentation mechanism of primary crystals without the analysis of how the critical crack length has been achieved. Fig. 12 compares the images of the fragmentation of the primary Al_3Ti crystal, i.e. Fig. 3(e), with the schematic of Mode I loading of a double edge notched plate. It appears that the simplest scenario of considering the final brittle fragmentation of primary crystals in the current analysis is Mode I fracture. As a consequence, the postulated fracture criterion is [27]

$$K_{Ic} = C\sigma\sqrt{\pi a_c} \quad (2)$$

where K_{Ic} is the fracture toughness, C is a constant (1.12 for small cracks), σ is the stress and a_c is the critical crack length.

The mechanical properties, particularly the fracture strength and toughness, of intermetallics are not readily available in open literature in the form that is required for accurate calculations. We have studied a large number of reference sources and extracted some data that could be useful in the preliminary assessment of fracture behaviour. These data are in many cases contradictory and obtained by different methods. For example, Yamaguchi et al. [28] measured fracture strength of around 160 MPa for polycrystalline DO_{22} Al_3Ti while Milman et al. [29] reported a value of 980 MPa for similar polycrystalline Al_3Ti at room temperature. Most recently, Wei et al. [30] also reported the fracture strength of polycrystalline Al_3Ti varying from 594 to 901 MPa. A possible reason for the discrepancy in the values may arise from the quality of the prepared Al_3Ti intermetallic samples, mainly including porosity, impurities and grain size. On the other hand, there are some data [31–33], especially on the fracture toughness, for the modified polycrystalline Al_3Ti phase which has a cubic L1_2 crystal structure but normally contains certain amount of a third element. The measured values of fracture toughness range from 2 to 3 $\text{MPa m}^{1/2}$. Moreover, the investigations [34,35] on the fracture toughness and strength of a polycrystalline Al_3Nb which has the same DO_{22} crystal structure as Al_3Ti found that the fracture toughness is $2.5 \pm 0.5 \text{ MPa m}^{1/2}$ and the fracture strength is around 900 MPa. With taking into account the similarities in properties and reported data, we can assume that the fracture toughness of primary Al_3Ti crystal is in the range from 2 to 3 $\text{MPa m}^{1/2}$ and the fracture strength is close to or perhaps slightly above 900 MPa. Based on the above assumptions, the critical crack length, a_c , of a primary Al_3Ti crystal was calculated using Eq. (2) with a range of stresses from 10 to 2000 MPa, and presented in Fig. 13(a). In addition, it is assumed that the maximum subcritical crack length is approximately 10% of the total width of the primary Al_3Ti crystal, i.e. 22 μm . This is based on the traces of dark lines that could be considered as the subcritical cracks (circled in Fig. 12(a) which records the very frame before the final fragmentation) and the length of these cracks is around 22 μm . As a consequence, for this critical crack size the minimum stress required to fragment the primary Al_3Ti crystal is between 215 and 322 MPa. The magnitude of this calculated minimum stress is in the same order as the pressure produced upon the collapse and rebound of an acoustic bubble in the neighbourhood of a solid boundary [36–39]. In contrast, the pressures at the bubble wall during its steady oscillation in water have a maximum value of 10 MPa [40] which requires a crack with the critical length larger than $10^4 \mu\text{m}$ which is not applicable to the observed cases.

The fracture strength of single crystal (both bulk and thin-film) silicon [41,42] has been reported to vary from 2 to 10 GPa depending on the specimen type, size, preparation, and test method. The measured values of the fracture toughness of single crystal silicon [43] range from

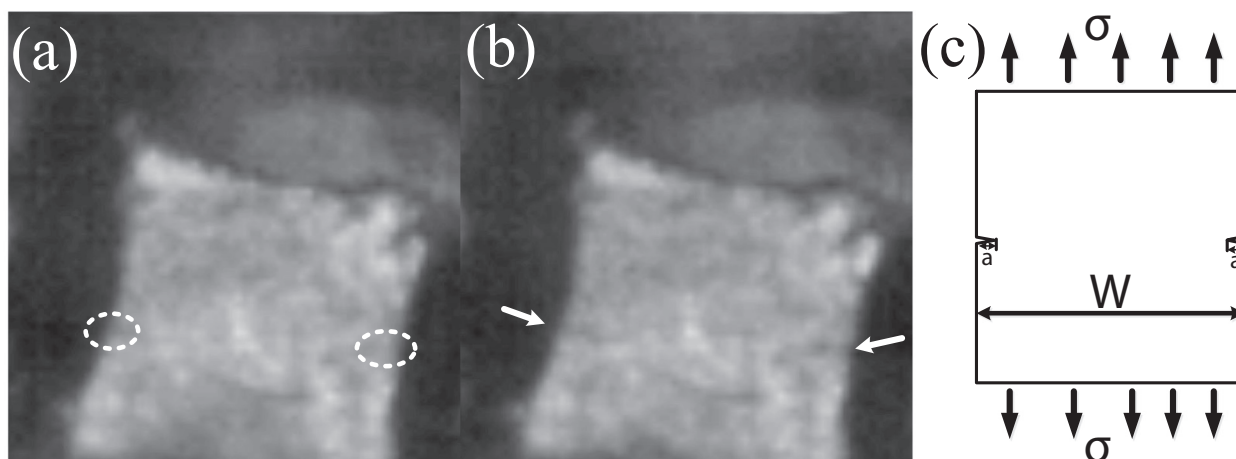


Fig. 12. (a) Image of a primary Al_3Ti crystal immediately before its fragmentation by a pulsating bubble, i.e., Fig. 3(e); (b) Image of the fragmentation of the primary Al_3Ti crystal where the crack is indicated by arrows, i.e. Fig. 3(f); (c) Schematic illustration of Mode I loading of a double edge notched plate [27].

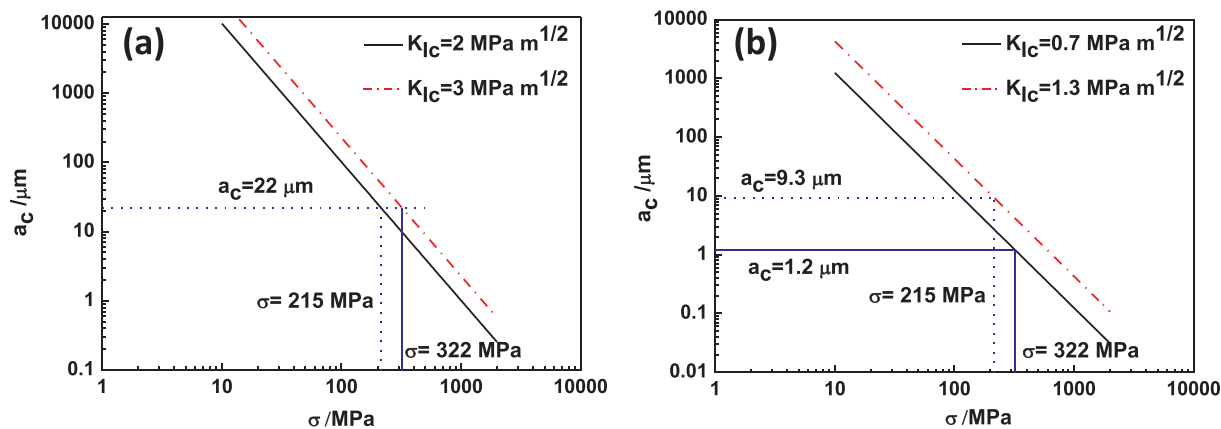


Fig. 13. (a) Critical crack length of primary Al_3Ti crystal; (b) critical crack length of primary Si crystal.

0.7 to 1.3 $\text{MPa m}^{1/2}$. Using these values, the critical crack length of primary Si crystal was calculated for a range of stresses as presented in Fig. 13(b). The stress calculated for the fracture of Al_3Ti and considered to be the stress inflicted by the cavitation bubble onto the primary crystal was used as an input parameter for Si fracture in order to obtain the maximum critical crack length in a Si crystal, as illustrated in Fig. 13(b). It can be seen that this critical crack length for primary Si ranges from 1 to 9 μm which is much smaller than that of primary Al_3Ti crystal. This explains a quicker fracture of Si that does not require a long stage of subcritical crack growth, something which could be expected due to the brittle nature of Si. A fracture mechanics analysis for primary Al_3V crystal was not carried out here since it has similar mechanical properties to primary Al_3Ti [44,45]. However, it can be inferred that the small dimensions and notch-like shape at the dendrite branch connection points/ roots of primary Al_3V crystal will only require a much smaller crack for fragmentation by the pressure exerted by either pulsating bubble or a travelling bubble cloud as implied from the fracture mechanics analysis of primary Al_3Ti crystal. This could explain the relatively easy fragmentation of primary dendritic Al_3V crystals observed in the current study.

It is important to mention again that the above fracture mechanics analysis is a rather rough estimation based on simple assumptions. More detailed fracture mechanics based on numerical simulation is necessary for advancing our understanding of the fragmentation mechanisms. Unfortunately the lack of reliable sets of mechanical properties of intermetallics still prevents us from accurate assessment of their fracture, either by analytical or numerical methods. It is rather difficult to experimentally obtain these properties due to the small sizes of the intermetallics. New methods such as nano-indentation accompanied by sophisticated heating system may be very useful in obtaining fracture toughness and strength information at high temperatures. In addition, it is also necessary to point out that the deep etching of the Al alloy samples to reveal the primary crystals may have introduced defects in the primary crystal which significantly reduces their integrity and hence their strength and toughness. Despite these acknowledged limitations of the experimental method, the authors believe that that the real-time, *in situ* high speed imaging observations presented in this paper provide significant insight into the possible mechanisms of particle fragmentation and subsequent refinement by USP in real molten alloys.

In the current experiments the primary particles are fixed in the Al matrix. This may be different from the case of real Al alloys in which the primary particles can also freely float in the liquid medium. However, as long as there is pressure that contributes to the propagation of pre-existing cracks in the primary particles, continuous interaction between the cavitation bubbles and primary particles would eventually lead to fragmentation by fatigue failure. Furthermore, considering the high frequency repetitions of cyclic pressures and the

short impact application duration, it is believed that the mechanism observed for the fixed primary particles is still valid in the case of freely-flowing particles in real Al alloys.

Based on the mechanisms observed in the current work, it is suggested that, in order to induce effective fragmentation of intermetallics in real Al alloys, ultrasonic processing should be applied during the growth stage of these intermetallics and the relative size of cavitation zone to the volume of Al melt need to be carefully considered.

4. Concluding remarks

High-speed imaging was used for studying *in situ* the dynamic interactions between cavitation bubbles and primary crystals formed in Al alloys. A simple but efficient method was developed based on deep etching of different Al alloys containing the primary crystals and ultrasonic processing of these deeply etched samples in water. Three very common primary crystals, i.e. Si, Al_3Ti , and Al_3V , with different morphologies and mechanical properties were investigated. By analysing the images extracted from the videos, the fragmentation mechanisms were revealed in much detail. In general, there are three major mechanisms by which the primary crystals are fragmented by the ultrasonic cavitation bubbles. The first fragmentation mechanism is a relatively slow process via fatigue crack growth until the critical crack size is reached. The pulsating cavitation bubbles bend the primary crystals in a high-frequency cycle which causes cracks in the primary crystals to develop to a critical length with subsequent brittle fracture and fragmentation. The second mechanism is a sudden process due to the collapse of passing-by bubble cloud. The pressure produced upon the collapse of bubble cloud violently fragments the primary crystals. Although this process is relatively fast, it still requires a pre-crack to be formed under cyclic loading. The third one is monotonic bending brittle fracture as a result of the high pressure produced upon the collapse of bubble cloud and the crack formation at the weak branch connection points. In addition, the fragmentation of the dendrite branches at roots due to the collision between two free-moving primary crystals was also observed, indicating that apart from mechanical properties, the morphology of the particles also play an important role in the actual fragmentation.

Acknowledgements

The authors acknowledge the financial support from UK Engineering and Physical Science Research Council (EPSRC) for the Ultra-Cast project (grant EP/L019884/1, EP/L019825/1, EP/L019965/1). The authors are also grateful to the Diamond Light Source Ltd for the loan of the high speed camera system.

Appendix A. Supplementary data

Supplementary data associated with this article can be found, in the online version, at <http://dx.doi.org/10.1016/j.ultsonch.2017.03.057>.

References

- [1] G.I. Eskin, D.G. Eskin, *Ultrasonic Treatment of Light Alloy Melts*, CRC Press, Boca Raton, Florida, 2015.
- [2] O.V. Abramov, *High-Intensity Ultrasonics: Theory and Industrial Applications*, Gordon and Breach Science Publishers, Amsterdam, The Netherlands, 1998.
- [3] G.I. Eskin, Broad prospects for commercial application of the ultrasonic (cavitation) melt treatment of light alloys, *Ultrason. Sonochem.* 8 (2001) 319–325.
- [4] L. Zhang, D.G. Eskin, L. Katgerman, Influence of ultrasonic melt treatment on the formation of primary intermetallics and related grain refinement in aluminum alloys, *J. Mater. Sci.* 46 (2011) 5252–5259.
- [5] G.M. Swallowe, J.E. Field, C.S. Rees, A. Duckworth, A photographic study of the effect of ultrasound on solidification, *Acta Metall.* 37 (1989) 961–967.
- [6] R. Chow, R. Blindt, A. Kamp, P. Grocutt, R. Chivers, The microscopic visualisation of the sonocrystallisation of ice using a novel ultrasonic cold stage, *Ultrason. Sonochem.* 11 (2004) 245–250.
- [7] R.M. Wagterveld, L. Boels, M.J. Mayer, G.J. Witkamp, Visualization of acoustic cavitation effects on suspended calcite crystals, *Ultrason. Sonochem.* 18 (2011) 216–225.
- [8] D. Shu, B. Sun, J. Mi, P.S. Grant, A high-speed imaging and modeling study of dendrite fragmentation caused by ultrasonic cavitation, *Metall. Mater. Trans. A* 43 (2012) 3755–3766.
- [9] Z. Guo, A.G. Jones, N. Li, S. Germana, High-speed observation of the effects of ultrasound on liquid mixing and agglomerated crystal breakage processes, *Powder Technol.* 171 (2007) 146–153.
- [10] D. Tan, T.L. Lee, J.C. Khong, T. Connolley, K. Fezzaa, J. Mi, High-speed synchrotron x-ray imaging studies of the ultrasound shockwave and enhanced flow during metal solidification processes, *Metall. Mater. Trans. A* 46 (2015) 2851–2861.
- [11] H. Huang, D. Shu, Y. Fu, J. Wang, B. Sun, Synchrotron radiation X-ray imaging of cavitation bubbles in Al–Cu alloy melt, *Ultrason. Sonochem.* 21 (2014) 1275–1278.
- [12] I. Tzanakis, W.W. Xu, D.G. Eskin, P.D. Lee, N. Kotsovinos, In situ observation and analysis of ultrasonic capillary effect in molten aluminium, *Ultrason. Sonochem.* 27 (2015) 72–80.
- [13] W.W. Xu, I. Tzanakis, P. Srirangam, W.U. Mirihanage, D.G. Eskin, A.J. Bodey, P.D. Lee, Synchrotron quantification of ultrasound cavitation and bubble dynamics in Al-10Cu melts, *Ultrason. Sonochem.* 31 (2016) 355–361.
- [14] M. Kang, H. Gao, D. Shu, J. Wang, F. Li, Y. Fu, L. Ling, B. Sun, In situ and real-time observation of the solidification process of Al-20 mass%Cu Alloy by synchrotron X-ray radiography, *Mater. Trans.* 55 (2014) 774–778.
- [15] E. Liotti, A. Lui, R. Vincent, S. Kumar, Z. Guo, T. Connolley, I.P. Dolbnya, M. Hart, L. Arnberg, R.H. Mathiesen, P.S. Grant, A synchrotron X-ray radiography study of dendrite fragmentation induced by a pulsed electromagnetic field in an Al-15Cu alloy, *Acta Mater.* 70 (2014) 228–239.
- [16] R.H. Mathiesen, L. Arnberg, X-ray radiography observations of columnar dendritic growth and constitutional undercooling in an Al-30wt%Cu alloy, *Acta Mater.* 53 (2005) 947–956.
- [17] D. Ruvalcaba, R.H. Mathiesen, D.G. Eskin, L. Arnberg, L. Katgerman, In situ observations of dendritic fragmentation due to local solute-enrichment during directional solidification of an aluminum alloy, *Acta Mater.* 55 (2007) 4287–4292.
- [18] P.D. Lee, J.D. Hunt, Hydrogen porosity in directional solidified aluminium-copper alloys: in situ observation, *Acta Mater.* 45 (1997) 4155–4169.
- [19] J. Mi, D. Tan, T.L. Lee, In situ synchrotron x-ray study of ultrasound cavitation and its effect on solidification microstructures, *Metall. Mater. Trans. B* 46 (2015) 1615–1619.
- [20] I. Tzanakis, G.S.B. Lebon, D.G. Eskin, K.A. Pericleous, Characterisation of the ultrasonic acoustic spectrum and pressure field in aluminium melt with an advanced cavitometer, *J. Mater. Process. Technol.* 229 (2016) 582–586.
- [21] I. Tzanakis, G.S.B. Lebon, D.G. Eskin, K.A. Pericleous, Characterizing the cavitation development and acoustic spectrum in various liquids, *Ultrason. Sonochem.* 34 (2017) 651–662.
- [22] F. Wang, D. Eskin, T. Connolley, J. Mi, Effect of ultrasonic melt treatment on the refinement of primary Al₃Ti intermetallic in an Al–0.4Ti alloy, *J. Cryst. Growth* 435 (2016) 24–30.
- [23] http://www.bendarygroup.com/images/instruction_manual_up200_400s_2007_ultrasonics.pdf.
- [24] R. Mettin, Bubble structures in acoustic cavitation, in: *Bubble and particle dynamics in acoustic fields: modern trends and applications*, 2005, pp. 1–36.
- [25] T. Ikehara, T. Tsuchiya, Crystal orientation-dependent fatigue characteristics in micrometer-sized single-crystal silicon, *Microsystems Nanoengineering* 2 (2016) 16027.
- [26] B.W. Zeiger, K.S. Suslick, Sonofragmentation of molecular crystals, *J. Am. Chem. Soc.* 133 (2011) 14530–14533.
- [27] M. Janssen, J. Zuidema, R. Wanhill, *Fracture Mechanics*, Second Edition, Taylor & Francis, 2004.
- [28] M. Yamaguchi, Y. Umakoshi, T. Yamane, Plastic deformation of the intermetallic compound Al₃Ti, *Philos. Mag. A* 55 (1987) 301–315.
- [29] Y.V. Milman, D.B. Miracle, S.I. Chugunova, I.V. Voskoboinik, N.P. Korzhova, T.N. Legkaya, Y.N. Podrezov, Mechanical behaviour of Al₃Ti intermetallic and L₁2 phases on its basis, *Intermetallics* 9 (2001) 839–845.
- [30] N. Wei, X. Han, X. Zhang, Y. Cao, C. Guo, Z. Lu, F. Jiang, Characterization and properties of intermetallic Al₃Ti alloy synthesized by reactive foil sintering in vacuum, *J. Mater. Res.* 31 (2016) 2706–2713.
- [31] E.P. George, J.A. Horton, W.D. Porter, J.H. Schneibel, Brittle cleavage of L₁2 trialuminides, *J. Mater. Res.* 5 (2011) 1639–1648.
- [32] E.P. George, D.P. Pope, C.L. Fu, J.H. Schneibel, Deformation and fracture of L₁2 trialuminides, *ISIJ Int.* 31 (1991) 1063–1075.
- [33] M.B. Winnicka, R.A. Varin, Microhardness and compressive mechanical behavior of L₁2 titanium trialuminides, *Metall. Trans. A* 24 (1993) 935–946.
- [34] C.P. Reip, G. Sauthoff, Deformation behaviour of the intermetallic phase Al₃Nb with DO₂₂ structure and of Al₃Nb-base alloys: Part I. Physical properties and short-term behaviour, *Intermetallics* 1 (1993) 159–169.
- [35] J.H. Schneibel, P.F. Becher, J.A. Horton, Microstructure and fracture toughness of powder-processed Al₃Nb, *J. Mater. Res.* 3 (1988) 1272–1276.
- [36] R. Hickling, M.S. Plesset, Collapse and rebound of a spherical bubble in water, *Phys. Fluids* 7 (1964) 7–14.
- [37] M.S. Plesset, R.B. Chapman, Collapse of an initially spherical vapour cavity in the neighbourhood of a solid boundary, *J. Fluid Mech.* 47 (1971) 283–290.
- [38] Y. Tomita, A. Shima, On the behavior of a spherical bubble and the impulsive pressure in a viscous compressible liquid, *Bull. JSME* 20 (1977) 1453–1460.
- [39] Y. Tomita, A. Shima, Mechanisms of impulsive pressure generation and damage pit formation by bubble collapse, *J. Fluid Mech.* 169 (1986) 535–564.
- [40] F.R. Gilmore, The Growth or Collapse of a Spherical Bubble in a Viscous Compressible Liquid, California Institute of Technology, Pasadena, CA, 1952, p. 41.
- [41] M.G. Mueller, M. Fornabaio, G. Žagar, A. Mortensen, Microscopic strength of silicon particles in an aluminium-silicon alloy, *Acta Mater.* 105 (2016) 165–175.
- [42] C.J. Wilson, A. Ormegegi, M. Narbutovskih, Fracture testing of silicon microcantilever beams, *J. Appl. Phys.* 79 (1996) 2386–2393.
- [43] C.P. Chen, M.H. Leopold, Fracture toughness of silicon, *Am. Ceram. Soc. Bull.* 59 (1980) 469–472.
- [44] Y. Umakoshi, M. Yamaguchi, T. Yamane, T. Hirano, M. Yamaguchi, Deformation and improvement of ductility of the intermetallic compounds Al₃V and Al₃(V, Ti), *Philosophical Magazine A: Physics of Condensed Matter, Structure, Defects and Mechanical Properties* 58 (1988) 651–665.
- [45] M. Yamaguchi, Y. Umakoshi, The deformation behaviour of intermetallic superlattice compounds, *Prog. Mater. Sci.* 34 (1990) 1–148.